

On the Use of Simulated Airborne Compact Polarimetric SAR for Characterizing Oil–Water Mixing of the Deepwater Horizon Oil Spill

Michael J. Collins, *Senior Member, IEEE*, Michael Denbina, *Student Member, IEEE*, Brent Minchew, Cathleen E. Jones, and Benjamin Holt

Abstract—Compact polarimetry (CP) synthetic aperture radar (SAR) is a form of coherent dual-pol SAR that has been shown to have great potential for maritime surveillance applications such as ship and ice detection. In this paper, we demonstrate the potential of CP data for oil spill characterization. As the availability of CP data is limited at this time, we simulate CP image data from UAVSAR L-Band quad-polarized images. We reconstruct quad-pol SAR data (termed pseudo-quad) from these simulated CP SAR data, and calculate an oil–water mixing index, termed Mdex. We show that the differences between the pseudo-quad and quad-pol Mdex maps are negligible. This contributes to the case that CP SAR has great potential for multiple applications in maritime surveillance.

Index Terms—Circular polarization, compact polarimetry (CP), oil spill, synthetic aperture radar (SAR).

I. INTRODUCTION

OIL SPILLS, such as the recent deepwater horizon oil spill in the Gulf of Mexico, are a significant environmental problem and pose a grave threat to animal and plant life in the regions they affect. Effectively responding to oil spills requires accurate and up to date information on the location, extent, and characteristics of the spill, but due to their unpredictable nature, and the fact that spills can spread to regions covering thousands of square kilometers, obtaining this information in a timely manner poses a challenge. Remote sensing is used operationally to map and monitor spilled oil [1]. While optical [2], including hyper spectral [3] and thermal [4] remote sensing may be used for this purpose, imaging radar, and in particular synthetic aperture radar (SAR) has received most of the attention due to its

Manuscript received June 30, 2014; revised October 27, 2014; accepted January 27, 2015. Date of publication March 15, 2015; date of current version March 27, 2015. The work of M. J. Collins was supported by the Natural Science and Engineering Research Council (NSERC) of Canada, and the Jet Propulsion Laboratory, Pasadena, CA, who sponsored his sabbatical visit.

M. J. Collins acknowledges funding support from Natural Science and Engineering Research Council (NSERC) of Canada, and the Jet Propulsion Laboratory who sponsored his sabbatical visit.

M. J. Collins and M. Denbina are with the Department of Geomatics Engineering, University of Calgary, Calgary, AB T2N 1N4, Canada (e-mail: michael.collins@ucalgary.ca).

B. Minchew is with the Seismological Laboratory, Division of Geological and Planetary Sciences, California Institute of Technology, 1200 East California Boulevard, Pasadena, CA 91125 USA.

C. E. Jones and B. Holt are with Jet Propulsion Laboratory, California Institute of Technology, 4800 Oak Grove Drive, Pasadena, CA 91109 USA.

Color versions of one or more of the figures in this paper are available online at <http://ieeexplore.ieee.org>.

Digital Object Identifier 10.1109/JSTARS.2015.2401041

all-weather, day/night imaging capability [1]. Backscatter from the sea surface is caused by a resonant interaction between the incident electromagnetic waves and short gravity and capillary waves on the sea surface [5]. In the presence of oil, these short water waves are significantly reduced leading to a concomitant reduction in backscatter [6].

Radar generally relies on the transmission and/or reception of multiple polarizations to infer information about the imaged surface. While early SAR systems used a single polarization channel (often HH or VV), it is generally acknowledged that multiple polarizations enhance the information of the characteristics of the ground [1].

The early research and resulting operational systems were based on single polarization, generally VV and SAR data. With the advent of fully polarimetric systems, recent research has explored these data [7]–[9]. Minchew *et al.* [10] have shown that various methods of polarimetric analysis, such as eigenvalue decomposition of the T_3 coherency matrix, can help to detect and analyze oil spills. However, while the added information contained in quad-polarized SAR data has been shown to have significant benefits, the reduced swath width implied by transmitting two polarizations compromises the operational advantage of quad-polarized data. Dual-polarized SAR has thus received recent attention for balancing the tradeoff between swath width and polarization diversity. One particular dual-polarized system, HH–VV, has received attention due to the sensitivity of the co-polarized phase difference in distinguishing oil from water, and oil from both oil “look-alikes” (biogenic slicks and other surfactants), and areas of low wind [9]. However, coherent HH–VV systems, since they transmit two polarizations, have the same swath-width constraints as quad-polarized systems. Minchew [11] recently developed an oil–water mixing index, called Mdex, which is based on HH and VV backscatter, and thus may be calculated from the two channels of an incoherent HH–VV dual-pol SAR system.

While most dual-pol SAR systems used for earth observation transmit a linear horizontal or vertical polarization, there has been much recent interest in compact polarimetric (CP) dual-pol systems that receive H and V, but transmit a “hybrid” polarization. For example, Raney [12] proposed the CL-pol or CTLR (circular transmit, linear receive) mode, where a circularly polarized wave is transmitted, and horizontal and vertical polarizations are received. CP SAR systems have been used in planetary imaging for some time. Most

recently, the miniSAR on board Chandrayaan-1 [13] collected CP SAR images of our moon [14], [15]. Evidence is accumulating that CP SAR data offer advantages over standard linear dual-pol data (HH–HV and VV–VH) for terrestrial applications such as crop classification [16], [17], soil moisture estimation [18], vegetation characterization [19], [20], and land cover mapping [17], [21], as well as maritime applications such as ship and iceberg detection [22], [23], and oil spill mapping [24]–[26].

Shirvany *et al.* [27] used the degree of polarization, a parameter derived from the CP Stokes vector, to detect oil spills, ships, and buoys using both dual-pol and CP data. His results, although encouraging, were purely qualitative. He found that for steep incidence angles, the dual-pol HH–HV mode produced the best oil spill detection results, while for shallow incidence angles, the best results were given by the coherent dual-pol HH–VV and CP modes, with the HH–VV being slightly superior to the CP data. It must be emphasized that to directly measure both HH and VV channels, a SAR system must either sacrifice the swath width benefits of being dual-pol (essentially becoming a quad-pol SAR system that discards two of its channels), or sacrifice the relative phase coherence between the HH and VV channels (as in Envisat’s alternating polarization mode). Thus, Shirvany’s HH–VV results are not operationally relevant to satellite-based surveillance.

More recently, Salberg *et al.* [25] explored the use of several parameters computed from compact polarity SAR for the detection of oil spills and the discrimination of oil spills from other causes of low backscatter, such as biogenic spills and low wind. They used the revised X-Bragg model, proposed by Iodice [28], as the context for calculating six different parameters from simulated compact polarity data. They found that the correlation coefficient between $HH + VV$ and $HH - VV$ (which they called “Coh,” for coherence) had the strongest performance when compared with the other CP metrics. However, it was weaker than the VV intensity and, in particular, had difficulty distinguishing crude oil from low wind. However, when three of the CP metrics (coherence, degree of polarization, and conformity index) were combined in a vector, the performance was superior to any individual metric, including VV , for both detection and discrimination between crude oil and other low backscatter regions.

Thus, compact polarity SAR offers significant potential in maritime applications, including the detection and characterization of oil spills, while offering the advantage, over quad-polarized systems, of wide swath imaging. In addition, Collins [29] demonstrated that the coherent co-polarized scattering vector may be accurately estimated from CP data over the ocean. Cross-polarized intensity may also be estimated, although the uncertainty is higher than for co-pol. Denbina and Collins [22] and Atteia and Collins [23] demonstrated that these reconstructed linear-pol elements may be used to detect icebergs and ships, and that detection using the reconstructed data actually outperforms the original linear-pol data. In this paper, we demonstrate that the linear polarizations reconstructed from simulated CP data may be used to accurately calculate Minchew’s Mdex oil–water mixing index. The CP data offer the additional advantage over both coherent dual-pol

linear systems (HH–HV and VV–VH) and over the incoherent HH–VV system, of superior performance for robust detection of both the spill edge, as well as ships that may be in the area.

While work has been done using CP data for the detection of oil spills, a slightly different but related issue is in characterizing the properties of oil spills once they have been detected. It is this characterization we focus on in this paper, using simulated CP data to reconstruct a pseudo quad-pol dataset [16] that consists of the pseudo-HH, pseudo-VV, and pseudo-HV intensities, as well as the HH–VV phase difference. We then use the pseudo-HH and pseudo-VV to calculate the oil–water mixing index, or Mdex, originally proposed by Minchew [11], in order to characterize the mixture of water and oil on the surface of the deepwater horizon oil spill. Since there are errors during the pseudo quad-pol reconstruction process, these will also manifest as errors in the final Mdex calculation. We therefore wish to assess the ability of compact polarimetric SAR to reproduce the oil–water mixing results of fully polarimetric data. Being able to measure the type of oil–water mixture on the surface of a spill is extremely helpful for both cleanup and containment operations.

In Section II, we introduce our methods of analysis, including a discussion of the data used, a review of the algorithms for reconstructing linear-pol from CP data, and a presentation of a revised Mdex algorithm. Section III presents our results, including a comparison of original and reconstructed linear-pol backscattering coefficients as a function of incidence angle, and a comparison of Mdex calculated from original and reconstructed data, both as histograms and images of Mdex and its components.

II. METHODS

A. Data

The Uninhabited Aerial Vehicle Synthetic Aperture Radar, or UAVSAR, is an L-band polarimetric SAR developed by the Jet Propulsion Laboratory and operated by Dryden Flight Research Center and the Jet Propulsion Laboratory.¹ The radar is designed to be operable on an UAV, but is currently mounted on a NASA Gulfstream III. The radar was specifically designed to acquire airborne repeat track SAR data for differential interferometric measurements. However, its quad-pol capability and low noise floor make it an excellent test bed for exploring L-band polarimetry. NASA sponsored the deployment of the UAVSAR to the Gulf of Mexico on June 22–23, 2010, for scientific studies of the main oil slick and the extent and impact of oil on coastal marshlands [30].

The UAVSAR operates with 80-MHz bandwidth from 1.2175 to 1.2975 GHz [31]. The radar transmits and receives in both horizontal (H) and vertical (V) (quad-polarization) modes. UAVSAR images a 22-km wide ground swath corresponding to an incidence angle range of 22°–65°. The UAVSAR noise equivalent σ^0 (NESZ) is -53 dB at its minimum near the mid-range of the swath [30]. The UAVSAR radar has 1.2 dB absolute calibration and 0.5 dB relative calibration between

¹UAVSAR data are freely available at the Alaska Satellite Facility (available: <https://www.asf.alaska.edu/>) and more information on the UAVSAR instrument can be obtained here (available: <http://uavsar.jpl.nasa.gov/>).

the amplitudes of the different polarization transmit/receive channels.

Note that the UAVSAR data has a very low noise floor, which is important for this application. In general, for the methodology in this paper to be valid, the σ^0 values for the HH and VV channels must be above the noise for both water and oil. A low noise floor is also helpful for the pseudo quad-pol reconstruction process (see Section II-B), due to the fact that the reconstruction process relies on accurately being able to estimate the HV σ^0 and subtracting it from the CP channels, such that cross-pol intensity must also be above the noise floor for the best reconstruction results. Note that our previous work on pseudo quad-pol reconstruction of ocean data used Radarsat-2 fine-quad mode data, which also has a very low NESZ compared to many spaceborne instruments (-30 dB and lower).

Two flight lines were used in this study were both collected on June 23, 2010: pass 14 010² (20:42 UTC), which passed directly over the Deepwater Horizon rig site at a heading of 140°; and pass 32 010³ (21:08 UTC), referred to as pass 32 010, which passed immediately to the west of and parallel to 14 010 along a 320° heading.

Mostly, this paper focuses on pass 14 010. All of the modeling we performed was using 14 010, and this is the pass used for all of the figures in this paper. At the end of the results section, we also report mean error and RMSE values for pass 32 010, for comparison.

UAVSAR single look complex products are processed with 1.7 m slant range resolution and 1 m azimuth (along-track) resolution. For this analysis, we used the multilook complex products available from the UAVSAR website, which have been processed with three range (cross track) and twelve azimuth (along track) looks and a pixel spacing of 5 m in slant range and 7.2 m in azimuth. All images shown in this paper are in slant range and azimuth coordinates. The transect plots in this paper are shown as a function of incidence angle and, in some cases, Bragg wavenumber. The incidence angle plotted is calculated for an untilted ocean surface. The relationship between slant range pixel number and incidence angle can be found in Minchew *et al.* [10].

Other relevant flight parameters for the UAVSAR overpasses of the Deepwater Horizon spill are given in Table I.

B. Pseudo Quad-Pol Reconstruction

For the CTLR compact polarity imaging mode, transmitting right circular polarization, the scattering vector is as follows:

$$k_{CTLR} = [S_{RH}, S_{RV}]^T \quad (1)$$

where “R” denotes that the transmitted polarization is right circular, and S is the complex scattering coefficient for the subscripted polarizations. This vector can also be rewritten entirely in the linear (H,V) basis as [21]

$$k_{CTLR} = \frac{1}{\sqrt{2}} [S_{HH} - iS_{HV}, -iS_{VV} + S_{VH}]^T. \quad (2)$$

²NASA file name: gulfco_14010_10054100_100623.

³NASA file name: gulfco_32010_10054_101_100623.

TABLE I
UAVSAR RADAR OPERATIONAL PARAMETERS

Parameter	Value
Center frequency	1.2575 GHz
Wavelength	0.2379 m
Bandwidth	80 MHz
Pulse duration	40 μ s
Operating altitude	12.5 km
Ground speed	220 m/s
Range swath	22 km
Look angle	22°–65°
Single look slant range resolution	1.7 m
Multilook slant range sample spacing	5 m
Single look azimuth resolution	1.0 m
Multilook azimuth sample spacing	7.2 m
Transmit power	3.1 kW
Cross pol isolation	-25 dB

We see that the scattering vector for a CTLR system essentially consists of the superposition of co-polarized (HH, VV) and cross-polarized (HV, VH) backscatter. This is an important result, because by making a number of assumptions, the co-polarized and cross-polarized information can be separated, allowing us to approximate quad-pol information using a dual-pol SAR system. This process, known as pseudo quad-pol (or pseudo-quad, or PQ) reconstruction, was originally developed by Souyris [16], expanded upon by Nord [21], and revised by Collins [29] for ocean scenes. The reconstruction of the quad-pol covariance matrix from simulated CTLR data is a two step process: 1) simulate the CTLR from linearly polarized quad-pol data; and 2) reconstruct elements of the quad-pol covariance matrix. Here, we summarize the basic process, which is discussed in detail in [29], then describe some of the challenges presented by the UAVSAR data and how we solved them.

From the CTLR scattering vector in (2), we can write the CTLR covariance matrix as a sum of three components

$$\begin{aligned} \mathbf{C}_{CTLR} = \frac{1}{2} \left\langle \left[\begin{array}{cc} |S_{HH}|^2 & i(S_{HH} \cdot S_{VV}^*) \\ -i(S_{VV} \cdot S_{HH}^*) & |S_{VV}|^2 \end{array} \right] \right. \\ + \left[\begin{array}{cc} |S_{HV}|^2 & -i|S_{HV}|^2 \\ i|S_{HV}|^2 & |S_{HV}|^2 \end{array} \right] \\ \left. + \left[\begin{array}{cc} -2\mathcal{I}(S_{HH} \cdot S_{HV}^*) & S_{HH} \cdot S_{HV}^* + S_{VV}^* \cdot S_{HV} \\ S_{HH}^* \cdot S_{HV} + S_{VV} \cdot S_{HV}^* & 2\mathcal{I}(S_{VV} \cdot S_{HV}^*) \end{array} \right] \right\rangle \quad (3) \end{aligned}$$

where the angle brackets represent spatial averaging and \mathcal{I} is the imaginary part of a complex number. Note that many of the discussions of the reconstruction algorithm in the literature assume that the 1/2 in front of the covariance matrix has been dropped off, for ease of calculation, and we will do the same here. Therefore, \mathbf{C}_{CTLR} should be multiplied by 2 before beginning the reconstruction process. In order to estimate the quad-pol 3×3 covariance matrix, we must estimate nine unknowns. However, we have only four equations from the CP mode covariance matrix. Thus, we must make some assumptions to constrain the solution space and reduce the number of unknowns and/or increase the number of equations. The original CP reconstruction algorithm [16] starts with the

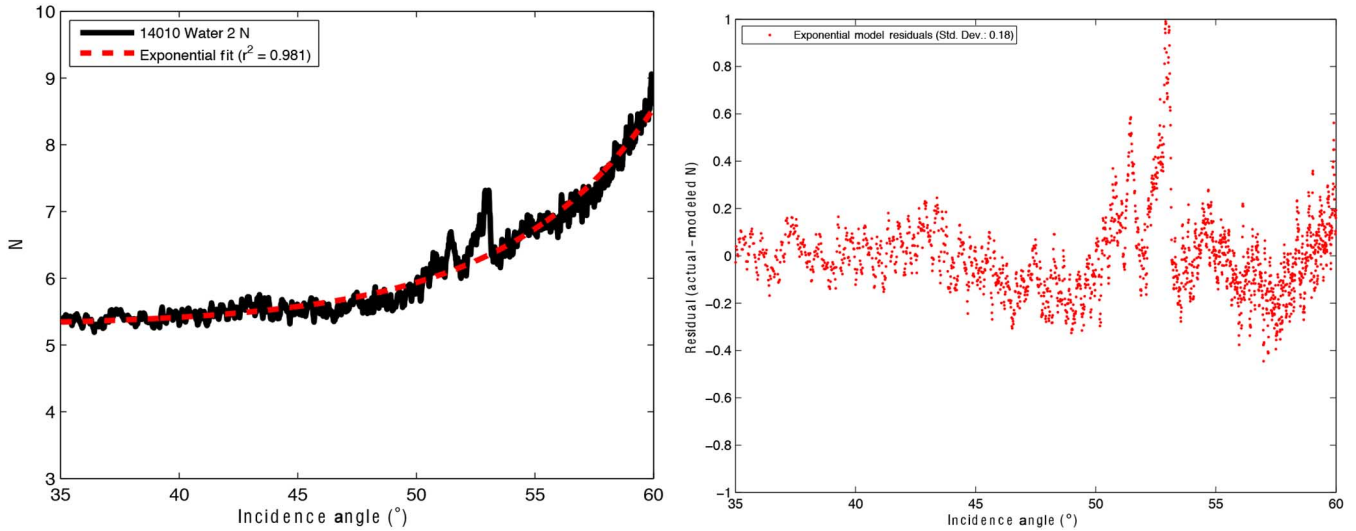


Fig. 1. Left-hand graph shows the profile of mean N (from line 14 010, averaged across the azimuth lines of the clean water segment) and modeled N (from the exponential regression) versus incidence angle. The graph on the right shows the residuals of the exponential model. Residuals calculated as (data model). The standard deviation of the residuals is 0.18. The exponential model has equation $y = 5.29 + 3.26 \times \exp(-x/6.21)$, where $x = 60 - \theta$, and θ is the incidence angle in degrees.

assumption of reflection symmetry, which has been validated for ocean backscatter at C-band [29].

Reflection symmetry is a property of media that are symmetric with respect to the incidence plane (see Fig. 1 of Souyris [16]) [32], [33], which is consistent with many terrestrial imaging scenarios as well as imaging of the ocean in the upwind or downwind directions. Reflection symmetry implies complete decorrelation between the co-polarized and cross-polarized backscattering coefficients, i.e.,

$$\langle S_{HH} S_{HV}^* \rangle = \langle S_{HV} S_{VV}^* \rangle = 0. \quad (4)$$

We tested the reflection symmetry assumption (see Appendix) and found that the effects of reflection asymmetry can be reduced, but not eliminated, if we perform further spatial averaging (in addition to the multilooking in the original data) as a preprocessing step. We found that a 5×5 -pixel averaging window was sufficient, since larger windows have diminishing returns in terms of the reduction in reflection asymmetry that they provide (see Fig. 13), and there is a minimum amount of reflection asymmetry present in this data which cannot be removed by spatial averaging. Removing the effects of the reflection asymmetry on the oil spill analysis was a key challenge for this study and will be discussed in more detail in Section II-C.

The reflection symmetry assumption simplifies the PQ covariance matrix, by removing the third component, reducing the number of unknowns to five: $|S_{HH}|^2$, $|S_{HV}|^2$, $|S_{VV}|^2$, and the real and imaginary parts of $(S_{HH} \cdot S_{VV}^*)$.

To further constrain the solution, Souyris developed a general relation between the linear HH–VV coherence and the cross-polarization ratio [16]

$$\frac{\langle |S_{HV}|^2 \rangle}{\langle |S_{HH}|^2 \rangle + \langle |S_{VV}|^2 \rangle} = \frac{(1 - |\rho|)}{N}. \quad (5)$$

The angle brackets represent spatial averaging and ρ is the HH–VV coherence, defined as

$$\rho \equiv \frac{\langle S_{HH} \cdot S_{VV}^* \rangle}{\sqrt{\langle |S_{HH}|^2 \rangle \cdot \langle |S_{VV}|^2 \rangle}}. \quad (6)$$

Souyris *et al.* [16] proposed this relation based on the idea of polarization state extrapolation. Specifically, when the HH–VV coherence magnitude is very high ($|\rho| \approx 1$), generally the cross-pol backscatter will be very low ($|S_{HV}|^2 \approx 0$). In the opposite case, when $|\rho| \approx 0$, the backscatter coefficients no longer depend on the polarization state, such that $|S_{HH}|^2 \approx |S_{VV}|^2 \approx 2|S_{HV}|^2$. Souyris *et al.* extrapolated a linear behavior between these two extremes, and as a result fixed N to a constant value of 4. This is consistent with scattering from vegetation and many types of natural media, but not necessarily to ocean backscattering, such that we chose a different value of N estimated from the quad-pol data itself.

Equations (5) and (6) are iteratively solved to estimate $|S_{HV}|^2$ and the HH–VV coherence (ρ) (see [29] for details). The pseudo co-pol intensities ($|S_{HH}|^2$, $|S_{VV}|^2$) and their complex conjugate product ($S_{HH} \cdot S_{VV}^*$) are estimated directly from the covariance matrix elements of the CP mode and the estimated $|S_{HV}|^2$ value as follows:

$$|S_{HH}|^2 = C_{11} - |S_{HV}|^2 \quad (7)$$

$$|S_{VV}|^2 = C_{22} - |S_{HV}|^2 \quad (8)$$

$$S_{HH} \cdot S_{VV}^* = -iC_{12} + |S_{HV}|^2 \quad (9)$$

where C_{11} , C_{12} , and C_{22} are the elements of the CTRL covariance matrix. Note that the phase of $(S_{HH} \cdot S_{VV}^*)$ is equivalent to the co-polarized phase difference between the HH and VV channels. Thus, the covariance matrix of the

TABLE II
SUMMARY OF RECONSTRUCTION ERRORS FOR THE WATER SUBSET OF PASS 14 010

Dataset		HH (%)	VV (%)	HV (%)	$ \rho $	$angle(\rho)$ (°)
1 (Original)	Median error	-12.75	6.34	15.75	-1.02×10^{-2}	9.14
	std. dev.	4.67	1.65	7.80	1.02×10^{-2}	3.19
2 (Symmetric)	Median error	-2.82×10^{-2}	-5.34×10^{-3}	0.32	2.92×10^{-4}	-9.70×10^{-4}
	std. dev.	1.45	1.30	5.15	5.93×10^{-3}	0.246
3 (Modified N_{ra})	Median error	-10.80	6.60	0.39	-2.54×10^{-2}	9.11
	std. dev.	3.85	1.68	8.06	2.04×10^{-2}	3.18
4 (Final model)	Median error	-2.10×10^{-2}	7.01×10^{-3}	0.39	-4.37×10^{-2}	9.11
	std. dev.	3.65	1.69	8.06	2.24×10^{-2}	3.18

Dataset 1 shows the median and standard deviation of the errors using the actual CTLR covariance matrix and the original reconstruction algorithm. Dataset 2 shows the errors when using a forced reflection symmetric covariance matrix. Dataset 3 shows the errors using the modified N_{ra} equation as in Section II-C. Dataset 4 shows the results when using the modified N_{ra} equation and a linear model to remove the reflection asymmetry terms from $|S_{HH}|^2$ and $|S_{VV}|^2$. The HH, HV, and VV intensity errors are percent errors, while $|\rho|$ and $angle(\rho)$ are absolute errors (the error for $angle(\rho)$ is in degrees), where the quad-pol value is greater than the reconstructed value, this is defined as a positive error. Errors are shown for reconstructed pixels only, which make up 98%+ of the total pixels.

pseudo quad-pol data derived from the CTLR CP mode can be written as

$$\mathbf{C}_{PQ_{CTLR}} = \begin{bmatrix} C_{11} - |S_{HV}|^2 & 0 & -iC_{12} + |S_{HV}|^2 \\ 0 & 2|S_{HV}|^2 & 0 \\ (-iC_{12} + |S_{HV}|^2)^* & 0 & C_{22} - |S_{HV}|^2 \end{bmatrix}. \quad (10)$$

The variable N in (5) is a crucial parameter in reconstructing the quad-pol covariance matrix. It is an index of agreement between $(1 - \rho)$ and the term on the cross-polarization ratio. In this study, we use an empirical model for N as described in [29], where it was shown that there is a strong and robust relationship between the mean N (\bar{N}) and the incidence angle of the scene for ocean Radarsat-2 fine-mode quad-pol scenes. A weak dependence on wind speed was also noted. We have applied this N model to the detection of both icebergs [22] and ships [23].

For Radarsat-2 scenes, the incidence angle changes by about 1° across the swath, so a single value of N may be used in the reconstruction of an entire scene. For UAVSAR data, the incidence angle varies from less than 35° to greater than 65° across its swath [31]. Thus, we must develop an N model that varies across the swath.

To build a model for N , we used the UAVSAR quad-pol data for the segment of clean water in pass 14 010 [10], located at azimuth lines 1700–2000, and confined our analysis to incidence angles between 35° and 60° , to ensure the dominance of Bragg scattering.

Using the quad-pol data, we calculated an N value for each pixel, then averaged all the pixels at each range line to produce a mean N for that range line. Then, we calculated the incidence angle of each range line, and created a profile of N versus incidence angle across the water subset. We used the same exponential model we used in our earlier work [29]

$$y = a + b * \exp(-x/c) \quad (11)$$

with $x = 60 - \theta$ as the independent variable, where θ is the incidence angle in degrees for an untilted ocean. The results are shown in Fig. 1 (left) with the residuals shown on the right.

The pattern of the residuals clearly shows that the empirical model is not able to reproduce the slant range oscillations in the data, particularly the spikes around 50° – 55° . However, the residuals are quite small and the overall standard deviation is only 0.18, so we originally used this simple model for our work (before refining it as described in the next section). The fitted parameters of this model are $a = 5.29$, $b = 3.26$, and $c = 6.21$.

We started by estimating N from the exponential model in 11 and then followed the reconstruction algorithm outlined above. However, we discovered that the HV estimates diverged for some pixels. We solved this problem by averaging the HV estimate from the current and previous iterations, thus smoothing the HV estimates. All HV estimates converged after this. The reconstruction errors are given in case 1 of Table II. Density plots of the reconstructed parameters versus quad-pol data are shown in Fig. 2. Note the bias in the HV and $|\rho|$ density plots, and the slight distortion in the ρ angle plot.

We then performed pseudo-quad reconstruction on a forced reflection symmetric CTLR covariance matrix (residue term set to zero), to show the ideal reconstruction results one could expect in the absence of reflection asymmetry. These reconstruction errors are given as case 2 of Table II. One can see that most of the bias is removed (median errors are smaller) in the reflection symmetric data, and the standard deviation of the errors is reduced. As such, we noted that the majority of the error in the reconstruction process in this case was due to the reflection asymmetry, not to the error in N .

C. Compensating for Reflection Asymmetry

For our oil spill analysis, we are primarily concerned with the co-polarization ratio, $|S_{HH}|^2$ divided by $|S_{VV}|^2$. Unfortunately, as shown in the reconstruction error table, there are biases in the HH and VV estimates when using our original reconstruction algorithm (case 1 in Table II). To remove as much of the reflection asymmetry as possible, we modified the original reconstruction algorithm.

Because the value of N controls the resulting HV estimates from the reconstruction, we explored the possibility of using N

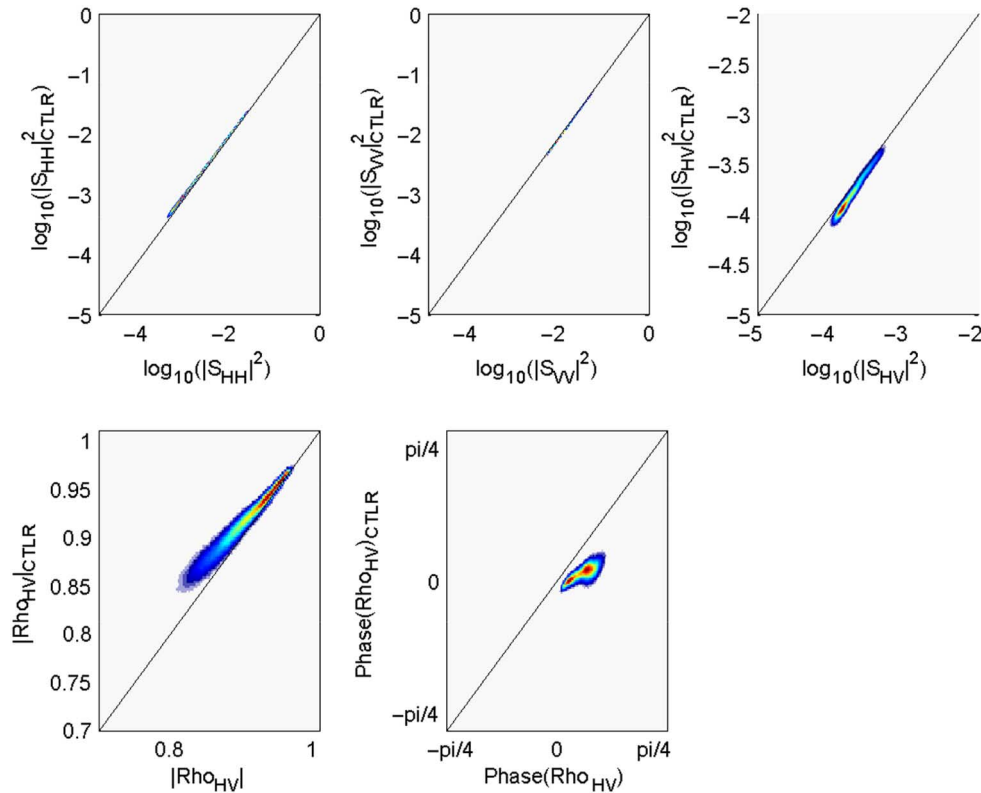


Fig. 2. Density plot of the reconstructed versus quad-pol values, for the water subset of pass 14 010.

to partially compensate for the reflection asymmetry by reducing the bias of the HV estimate. Note that this will only improve the HV results—since the reflection asymmetry is still part of the CTLR covariance matrix, it will still manifest in the HH, VV, and ρ results. Although the HV channel does not play a direct role in the subsequent calculation of an oil–water index, by removing the bias in the HV estimate, the remaining bias in the HH and VV estimates will result entirely from the values of $-2\mathcal{I}(S_{HH} \cdot S_{HV}^*)$ and $2\mathcal{I}(S_{VV} \cdot S_{HV}^*)$, respectively [see (3)], which can then be isolated. The HV channel is also very useful for many other maritime surveillance applications, being closely related to wind speed [34], so removing the bias from its estimates is also helpful in that respect.

To do this, we propose a slightly different formulation of N that we will refer to as N_{ra} (reflection asymmetric N), one that essentially calculates what the value of N would be from “perfectly reconstructed” (zero HV error) but reflection asymmetric data. Recall that N is normally calculated as

$$N = (1 - |\rho|) \cdot \frac{|S_{HH}|^2 + |S_{VV}|^2}{|S_{HV}|^2}. \quad (12)$$

Such that we can also calculate a modified N_{ra} as follows:

$$N_{ra} = \left(1 - \left| \frac{-iC_{12} + |S_{HV}|^2}{\sqrt{(C_{11} - |S_{HV}|^2) \cdot (C_{22} - |S_{HV}|^2)}} \right| \right) \times \frac{(C_{11} - |S_{HV}|^2) + (C_{22} - |S_{HV}|^2)}{|S_{HV}|^2} \quad (13)$$

where C_{ab} is the element of the CTLR covariance matrix in row a and column b . For reflection symmetric data, (12) and

(13) would be equivalent. We calculated N_{ra} values using (13) for the same segment of clean water in pass 14 010 (azimuth lines 1700–2000) and averaged them across azimuth lines, then plotted them versus incidence angle and performed a similar regression as for the original N values. The results are shown in Fig. 3. The modified N_{ra} values, compared to the original N values, are significantly more consistent across the swath (note that Figs. 1 and 3 have the same axes). For this reason, instead of using an exponential model, we used a constant value of N_{ra} equal to the mean value, which was $\bar{N}_{ra} = 4.2923$.

Using this constant N value, the reconstruction was performed again. The errors are shown as case 3 in Table II. Note that the HV bias has been significantly reduced. However, the biases in many of the other parameters increase, or remain similar—previously, the HV estimate was “absorbing” some of the reflection asymmetry, but this is no longer the case. The bias in the HH and VV intensities, which we are most concerned about for this study, is still quite large. To compensate for this, we rewrite the equations used to calculate the pseudo HH and VV estimates and relax the reflection symmetry assumption

$$|S_{HH}|^2 = C_{11} - [|S_{HV}|^2 - 2\mathcal{I}(S_{HH} \cdot S_{HV}^*)] \quad (14)$$

$$|S_{VV}|^2 = C_{22} - [|S_{HV}|^2 + 2\mathcal{I}(S_{VV} \cdot S_{HV}^*)]. \quad (15)$$

For convenience, we will refer to $-2\mathcal{I}(S_{HH} \cdot S_{HV}^*)$ as the HH asymmetry term, and $2\mathcal{I}(S_{VV} \cdot S_{HV}^*)$ as the VV asymmetry term. The values of these terms vary between water and oil pixels, which poses a problem for modeling their behavior. However, when normalizing them by the total backscattered power, i.e., the span of \mathbf{C}_{CTLR} , which is equal to $C_{11} + C_{22}$,

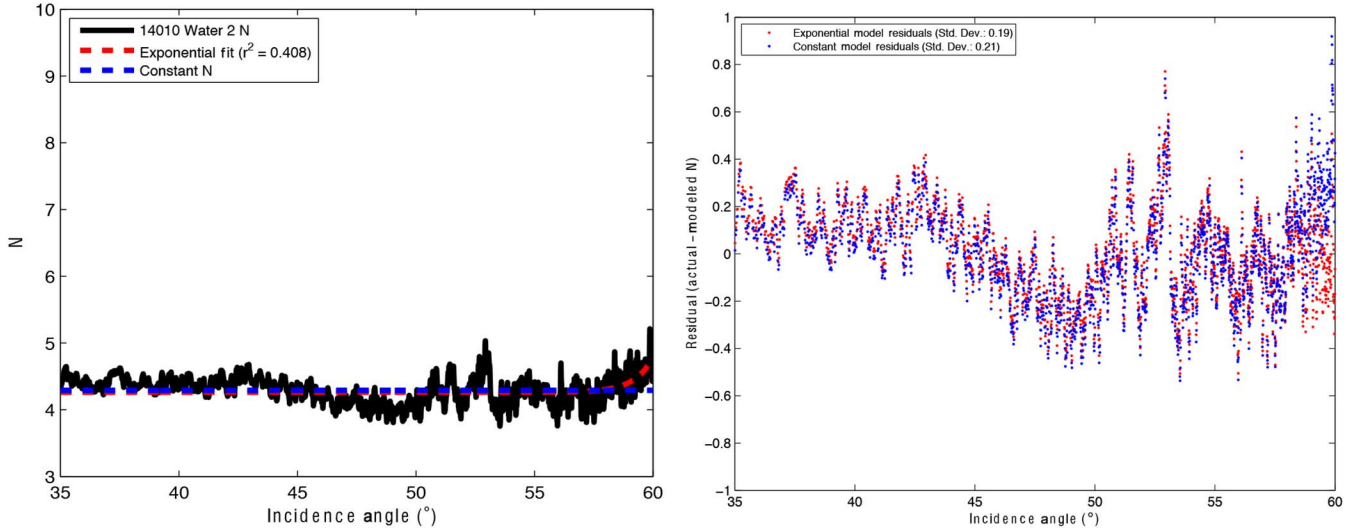


Fig. 3. Left-hand graph shows the profile of mean N_{Tra} (from line 14 010, averaged across the azimuth lines of the clean water segment) and modeled N_{Tra} (from the exponential regression) versus incidence angle. The graph on the right shows the residuals of the exponential model. Residuals calculated as (data - model). The standard deviation of the residuals is 0.19. The exponential model has equation $y = 4.26 + 0.522 \times \exp(-x/0.795)$, where $x = 60 - \theta$, and θ is the incidence angle in degrees.

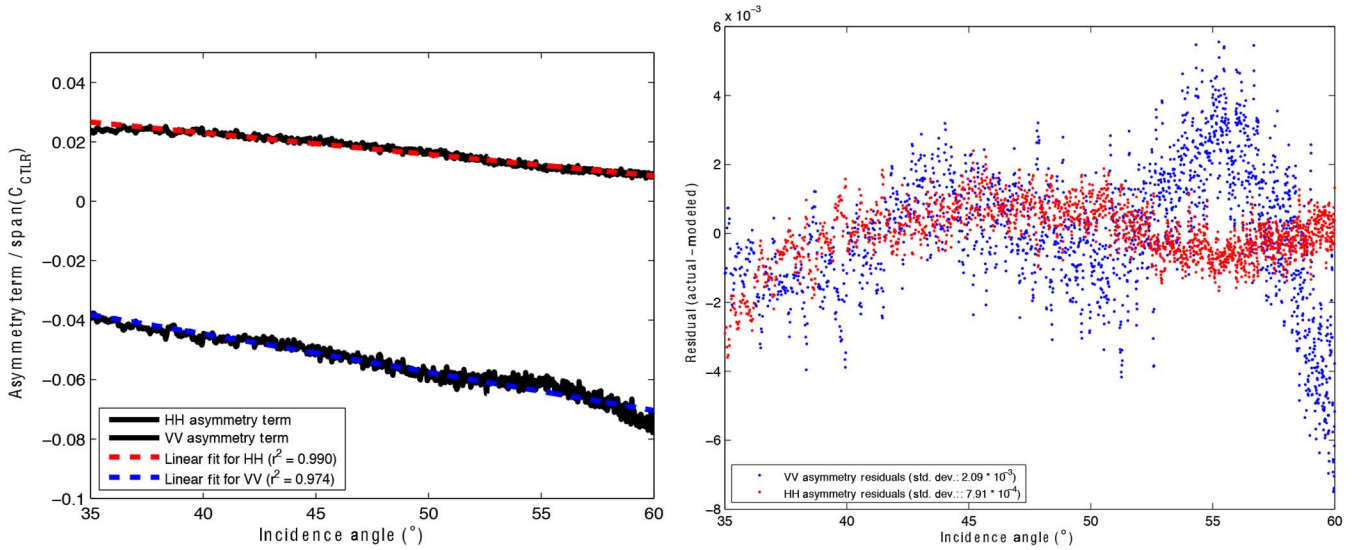


Fig. 4. Left-hand graph shows a profile of the HH and VV asymmetry terms, divided by the span of the CTLR covariance matrix, plotted versus incidence angle and modeled with a line. The graph on the right shows the residuals of the linear models. Residuals calculated as (data - model), with standard deviations shown on the legend. The HH asymmetry model has equation $y = -0.0007235\theta + 0.05194$, and the VV asymmetry model has equation $y = -0.001289\theta + 0.006949$.

this behavior is reduced. Similar to our modeling of N , we calculated the mean value (across azimuth lines) of these two asymmetry terms divided by the total backscattered power, then plotted the result versus incidence angle for the 14 010 water subset. We then modeled these normalized terms as linear functions of incidence angle. The results are shown in Fig. 4. Using those linear models, we calculated new HH and VV estimates using the following equations:

$$|S_{HH}|^2 = C_{11} - [|S_{HV}|^2 + (-0.0007235\theta + 0.05194)(C_{11} + C_{22})] \quad (16)$$

$$|S_{VV}|^2 = C_{22} - [|S_{HV}|^2 + (-0.001289\theta + 0.006949)(C_{11} + C_{22})]. \quad (17)$$

Density plots of this reconstruction versus the quad-pol data are shown in Fig. 5, and the reconstruction errors are shown as case 4 in Table II. The biases in HH, VV, and HV are all significantly reduced compared to the original reconstruction. ρ has become even more distorted, but has no bearing on the oil spill analysis. It is likely that the reflection asymmetry in ρ could also be compensated for using a similar method, but we have not attempted this. This would be more challenging than compensating for the reflection asymmetry in HH and VV, since ρ is used to iteratively solve for HV, and therefore the reflection symmetry in ρ has an influence on the HV estimates as well as the estimate of itself.

Mean transects of σ^0 for both quad-pol and pseudo-quad data are shown in Fig. 6 for a section of clean water and a section of

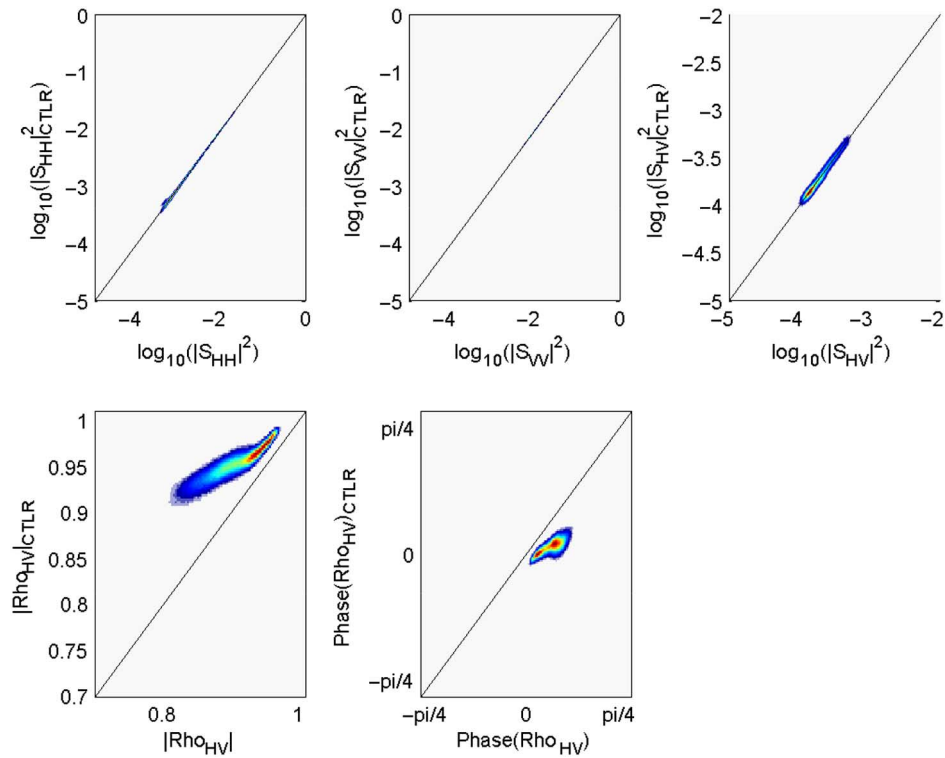


Fig. 5. Density plot of the reconstructed versus quad-pol values, for the final reconstruction, using the modified N_{ra} equation and reflection asymmetry compensation. Calculated for the water subset of pass 14 010.

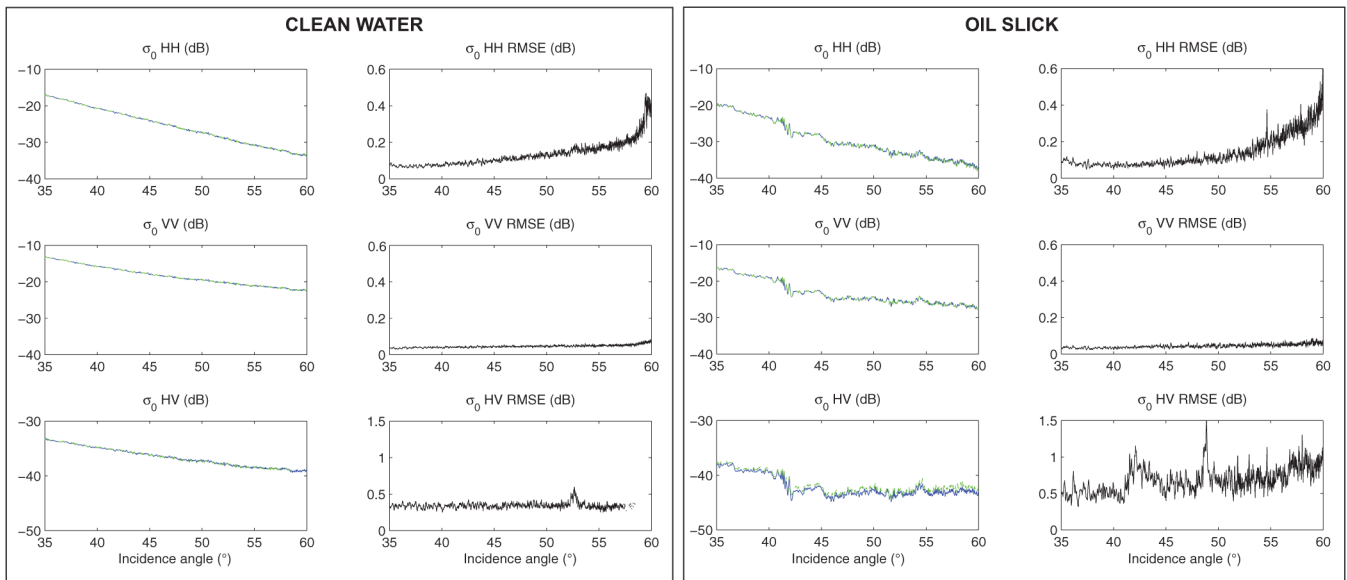


Fig. 6. Mean transects of σ^0 for a section of clean water (left-hand panel) and oil-covered water (right-hand panel).

oil-covered water. One can see that the reconstruction errors are less than 0.5 dB for the co-pol channels for both water and oil. The errors for the HV are less than 0.5 dB for water and somewhat more variable, but mostly less than 1 dB, for oil-covered water. Consistent with Table II, the reconstruction errors for HH are slightly higher than those for VV. In addition, it is evident that the reconstruction errors for VV are almost constant with incidence angle, showing a very slight increase

with incidence angle after about 58° for water (not for oil). The error in HH shows a steady increase from about 40° and up, becoming more variable as the incidence angle increases. Below 40° the error in HH is approximately constant, increasing slightly for oil-covered water. This will certainly affect the Mdex calculation—likely producing a slight deterioration in the Mdex error as the incidence angle increases, and perhaps below 40° .

D. Oil/Water Mixing Index: Mdex

After reconstructing the two co-pol channels from the simulated compact polarity data, we calculate the oil–water mixing index developed by Minchew [11]. This index is a rough estimate of the mixing of sea water and spilled crude oil. It is intended to indicate whether the oil is mixed with the sea water, or whether it is a viscoelastic oil film on the surface. Knowing whether oil is mixed or floating on the surface as a film is useful for cleanup operations, assessments of the environmental impact of oil spills, and studies of the behavior of contaminants on the sea surface. The standard advantages of SAR imaging (day/night, all-weather) make them well-suited to oil spill response so long as useful metrics, such as extent of contamination and degree of mixing, can be gleaned from the data.

Before calculating Mdex, we “detected” the oil slick, i.e., classified the image into oil or clean water. As discussed in the introduction, oil detection with SAR is an active area of research reviewed recently by Brekke and Solberg [1]. A recent study by Salberg *et al.* [25] explored the detection of crude oil slicks using various metrics calculated from CP data. Zhang *et al.* [24] found the conformity index, calculated from CP, was useful in discriminating oil from clean water. In this study, we use the co-pol ratio, as was used in the original Mdex study. Since the damping effects of oil drive down the VV backscatter significantly, while having a smaller effect on HH backscatter, this ratio is very sensitive to oil. A recent study by Brekke *et al.* [26] found that this ratio is also very useful in detecting oil in ice-infested waters.

Numerous studies have shown that oil on the sea surface appears as areas of low backscatter power ($|S_{pq}|_{\text{oil}}^2 < |S_{pq}|_{\text{water}}^2$, where p and q are either H or V) in SAR images [5], [35]. There are primarily two ways by which oil can reduce the radar backscatter. First, oil can reduce the small-scale wind-driven surface roughness, relative to uncontaminated seawater under the same environmental conditions, causing a smaller percentage of the reflected radar energy to be directed back to the radar antenna. Second, if oil is mixed in high enough concentrations within a thin layer (a few millimeters for a radar wavelength of 24 cm) below the surface, the oil will reduce the effective dielectric constant of the ocean surface because the dielectric constant of oil is much lower than that of seawater. A lowered dielectric constant leads to less total energy reflected by the surface.

Radar backscatter power ($S_{pp}S_{pp}^*$) is proportional to the normalized radar cross section (NRCS) of a given scatterer. The NRCS for the ocean under moderate wind conditions can be modeled using a tilted Bragg scatter (or small-perturbation) model. This model treats the ocean surface as a composite of small facets that are tilted relative to local up. The facet tilt is governed by long-wavelength ocean waves and each facet carries shorter wavelength, wind-driven gravity-capillary waves whose amplitudes are much smaller than the radar wavelength. Scattering from this surface is caused by Bragg resonance, which is the result of constructive interference of radar waves scattered from roughness features whose spatial distribution corresponds to the wavenumber $k_{Bragg} = 2k_r \sin \theta_i$, where θ_i

is the radar incidence angle and k_r is the radar wavenumber in free space. The facet tilt is defined by two angles: ψ , which is the in-plane angle, i.e., between local up and the projection of the facet normal onto the scattering plane (the vertical plane that contains the radar line-of-sight), and ζ , which is the out-of-plane angle, i.e., the angle between local up and the projection of the facet normal onto the vertical plane that is orthogonal to the scattering plane. Then the incidence angle to a given facet is $\theta_i = \cos^{-1} [\cos(\theta + \psi) \cos(\zeta)]$, where θ is the incidence angle relative to the surface normal of the facet.

The co-polarized (HH or VV) NRCS for the tilted Bragg model is defined as

$$\sigma_{pp}^0 = 4\pi k_r^4 \cos^4 \theta_i \Gamma_{pp} W \quad (18)$$

where Γ_{pp} is the reflectivity for the p -polarized wave and W is the spectral density of the small-scale ocean roughness [35]–[37]. The reflectivity

$$\Gamma_{pp} = \left| \left(\frac{\sin(\theta + \psi) \cos \zeta}{\sin \theta_i} \right)^2 \alpha_{pp} + \left(\frac{\sin \zeta}{\sin \theta_i} \right)^2 \alpha_{qq} \right|^2 \quad (19)$$

where q indicates polarization ($p \neq q$). Γ_{pp} defines the total amount of energy that can be scattered from a given surface and is a function of the facet tilt and the Bragg scattering coefficients

$$\alpha_{HH} = \frac{\cos \theta_i - \sqrt{\varepsilon_r - \sin^2 \theta_i}}{\cos \theta_i + \sqrt{\varepsilon_r - \sin^2 \theta_i}} \quad (20)$$

$$\alpha_{VV} = \frac{(\varepsilon_r - 1) \{ \sin^2 \theta_i - \varepsilon_r [1 + \sin^2 \theta_i] \}}{(\varepsilon_r \cos \theta_i + \sqrt{\varepsilon_r - \sin^2 \theta_i})^2}. \quad (21)$$

The relative dielectric constant ε_r is taken to be

$$\varepsilon_r = \varepsilon_r^{\text{eff}} = w_o \varepsilon_r^{\text{oil}} + (1 - w_o) \varepsilon_r^{\text{water}} \quad (22)$$

where $\varepsilon_r^{\text{water}}$ and $\varepsilon_r^{\text{oil}}$ are the relative dielectric constants of seawater and crude oil, respectively, and w_o is the oil weighting factor. The weighting factor is proportional to the volumetric oil concentration where the constant of proportionality is defined by the shape factor of the oil (or water) inclusions (see [38], Vol. III, Appendix E).

Typical values for the real part of the dielectric constant of crude oil [39], [40] are a factor of 30–40 smaller than typical values for the dielectric constant of seawater [41]. This means that oil must be present in relatively high concentrations in order to significantly influence Γ_{pp} . Furthermore, the relatively low dielectric constant of crude oil means that scattering from a thin layer of crude oil is negligible compared to the scattering from the underlying sea surface. Therefore, oil can only reduce the effective dielectric constant if it is mixed to a depth on the order of the skin depth of the radar signal ($\delta_s = 1/k_r |\text{Imag}[\sqrt{\varepsilon_r}]|$).

Ascertaining the mixing characteristics of oil requires decoupling Γ_{pp} from W in (18). To do so, we first consider the co-polarized NRCS ratio ($\sigma_{HH}^0/\sigma_{VV}^0 = \Gamma_{HH}/\Gamma_{VV}$) for relatively clean water. This ratio, a function of only the dielectric

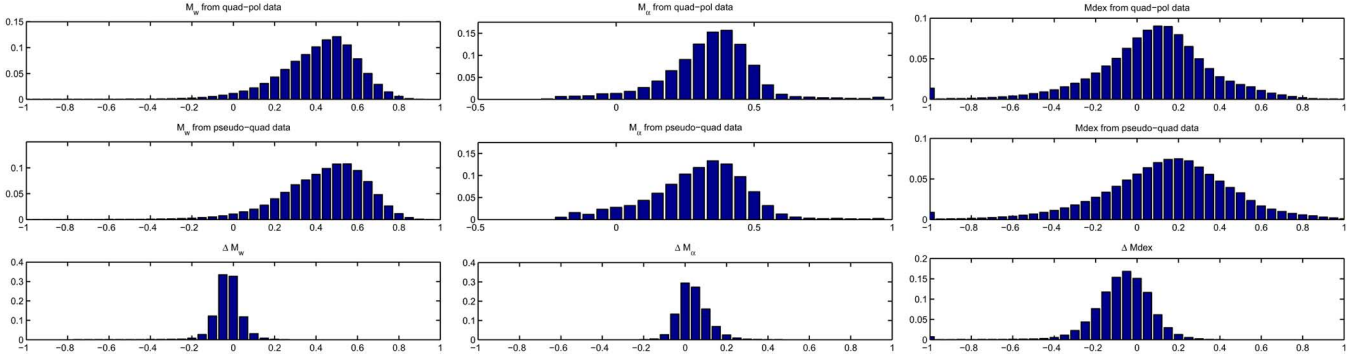


Fig. 7. Histograms of M_W (left column), M_α (center column), and M_{dex} (right column) for the quad-pol data (top row) and the reconstructed pseudo-quad (center row). The histogram of the difference is shown at bottom.

constant and the facet tilt, can be used to estimate the tilt angles ψ and ζ if we assume a reasonable value for the dielectric constant of sea water. In this case, ψ and ζ are estimated using the co-polarized NRCS ratio from the data and $\epsilon_r^{water} = 80 - 70i$. Because ψ and ζ are determined by long-wavelength ocean waves, which are assumed to be unaffected by the presence of oil, we can substitute the values of ψ and ζ into (19) through (21) and estimate the weighting factor w_o using a simple lookup table. We can then use w_o with (22) to invert (18) for W .

The values for w_o and W can then be used to calculate the mixing index, M_{dex} :

$$\begin{aligned}
 M_{dex} &= \frac{1}{\sigma_{VV}^{o(water)}} \left[\frac{\partial \sigma_{VV}^o}{\partial W} \Delta W - \frac{\partial \sigma_{VV}^o}{\partial \Gamma_{VV}} \Delta \Gamma_{VV} \right] \\
 &\approx \frac{W^{water} - W^{oil}}{W^{water}} - \frac{|\alpha_{VV}^{water}|^2 - |\alpha_{VV}^{oil}|^2}{|\alpha_{VV}^{water}|^2} \quad (23) \\
 &= M_W - M_\alpha
 \end{aligned}$$

which accounts for the difference in the relative contributions to the reduction in backscatter power from surface roughness damping (M_W) and signal attenuation (M_α). In (23), W^{water} is the surface roughness of relatively clean water taken as close to the oil as possible (at the same incidence angle), $|\alpha_{VV}^{water}|^2$ can be calculated from (21) using a reasonable value of ϵ_r^{water} , the Δ operator indicates the difference between the relatively clean ambient water and the oil slick. The left-hand term of (23), called M_W , represents the normalized damping factor. This term should vary between 0 (= no damping) and 1 (= total damping). The right-hand term M_α describes the normalized power attenuation factor, and also varies between 0 (= no attenuation) and 1 (= complete attenuation—such that $\epsilon_r^{eff} = 1$). M_α may be simplified using $|\alpha_{VV}|^2$ instead of Γ_{VV} because (19) reduces to only the α_{VV} term and its leading coefficient if we assume ζ is small and consider that $|\alpha_{VV}| > |\alpha_{HH}|$. Note that we use the VV polarization in (23) due to its higher signal-to-noise ratio.

An important assumption of the M_{dex} index is that the local wind forcing for the clean water reference is comparable to the oil covered water. Any differences in wind forcing between the oil slick and the clean water reference will lead to local variations in the roughness spectrum that may cause negative values for M_W . When M_{dex} is used operationally, these

negative values are set to zero [11]. Since the purpose of our research is to compare M_{dex} calculated with linear co-pol data with that calculated with CP data, we will not correct negative M_W values.

M_{dex} thus varies between -1 (for no damping and total attenuation) and 1 (for total damping and no attenuation), provided the winds in the study area are sufficient to stimulate ocean surface roughness. The sign of M_{dex} gives an indication of the presence of mixed oil versus a surface film. Positive M_{dex} values indicate areas primarily covered with a thin film, with a higher absolute M_{dex} value representing a greater degree of certainty as to the characteristics of the oil. Negative M_{dex} values, on the other hand, suggest that the oil is mixed in relatively high concentrations to a depth on the order of the skin depth of the radar signal. M_{dex} values near zero can result from oil that is mixed and has an overlying surface film, or in some cases, could suggest the presence of seawater inclusions in a crude oil mixture that is known as an emulsion.

III. RESULTS

The M_{dex} , M_α , and M_W values calculated using the pseudo-quad data are comparable to those obtained with the quad-pol data [11]. The histograms of the M_{dex} , M_W and M_α are shown in Fig. 7. Images of the VV σ^0 (in dB units) for the quad-pol data, the pseudo-quad data, and their difference, are shown in Fig. 8. The images for the M_{dex} index and its components are shown in Figs. 9–11. These results suggest that the pseudo-quad data provide as reliable a method of estimating the characteristics of spilled oil as original quad-pol data.

As shown in [11], there is a long left-hand tail in both M_W histograms. We have excluded pixels with $M_W < -1$ from further analysis here, due to the fact that these pixels are out of the range of valid M_W values (which should range from -1 to 1). These pixels represent less than 0.5% of the total, but they adversely affect the statistics due to their extreme outlier values. The mean M_W for the quad-pol data is 0.41 and for the pseudo-quad data is 0.44. One can see from the histogram of ΔM_W that the reconstructed pseudo-quad data overestimates M_W very slightly. The mean difference is -0.03 , and the RMSE is 0.084; thus, we can say that the pseudo-quad data provide a reliable estimate of M_W . From the M_W images, we can see that the spatial patterns in the quad-pol data are reproduced in

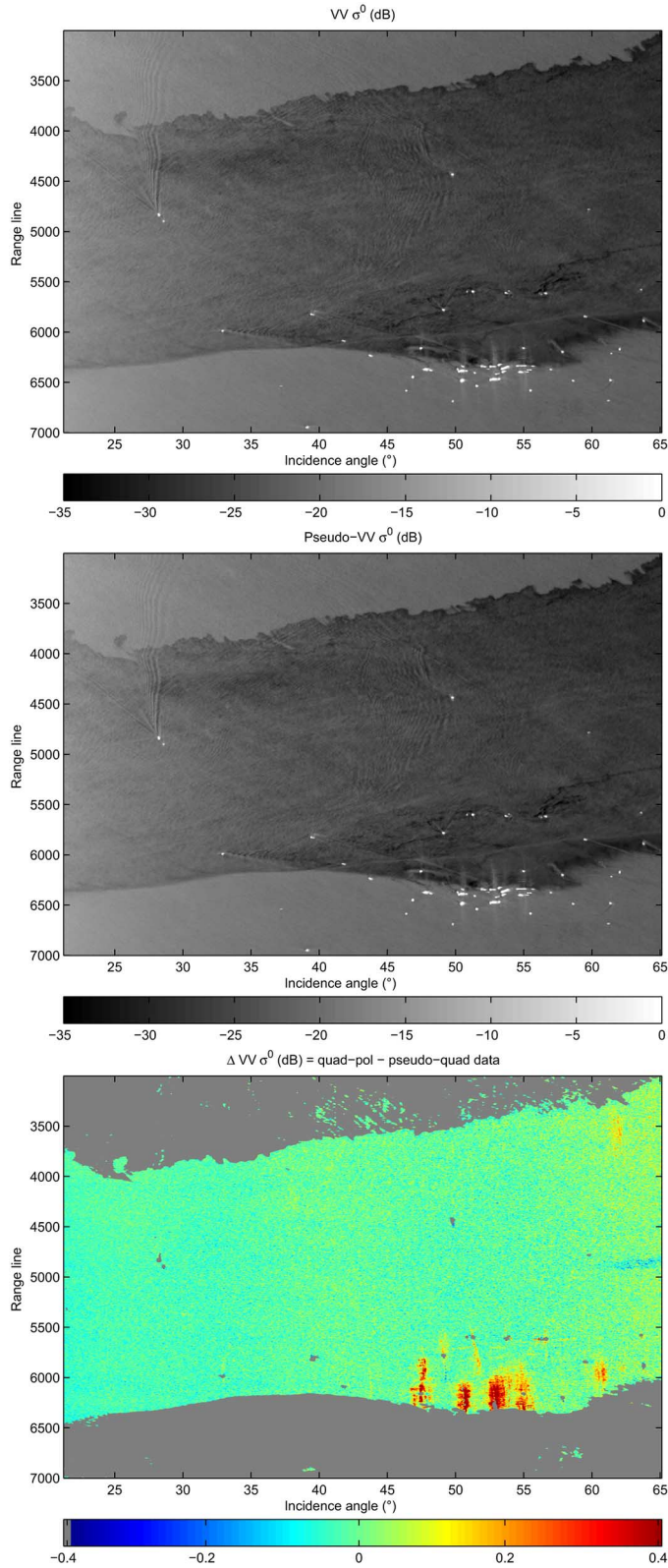


Fig. 8. Images of $VV \sigma^0$ (dB) for quad-pol data (top) and reconstructed pseudo-quad data (center). The difference image is shown at bottom.

the pseudo-quad image. The difference image suggests that the difference increases slightly for low- and high-incidence angles. This is likely due to our N_{ra} and reflection asymmetry models having a poorer fit to the data near the edges of the swath.

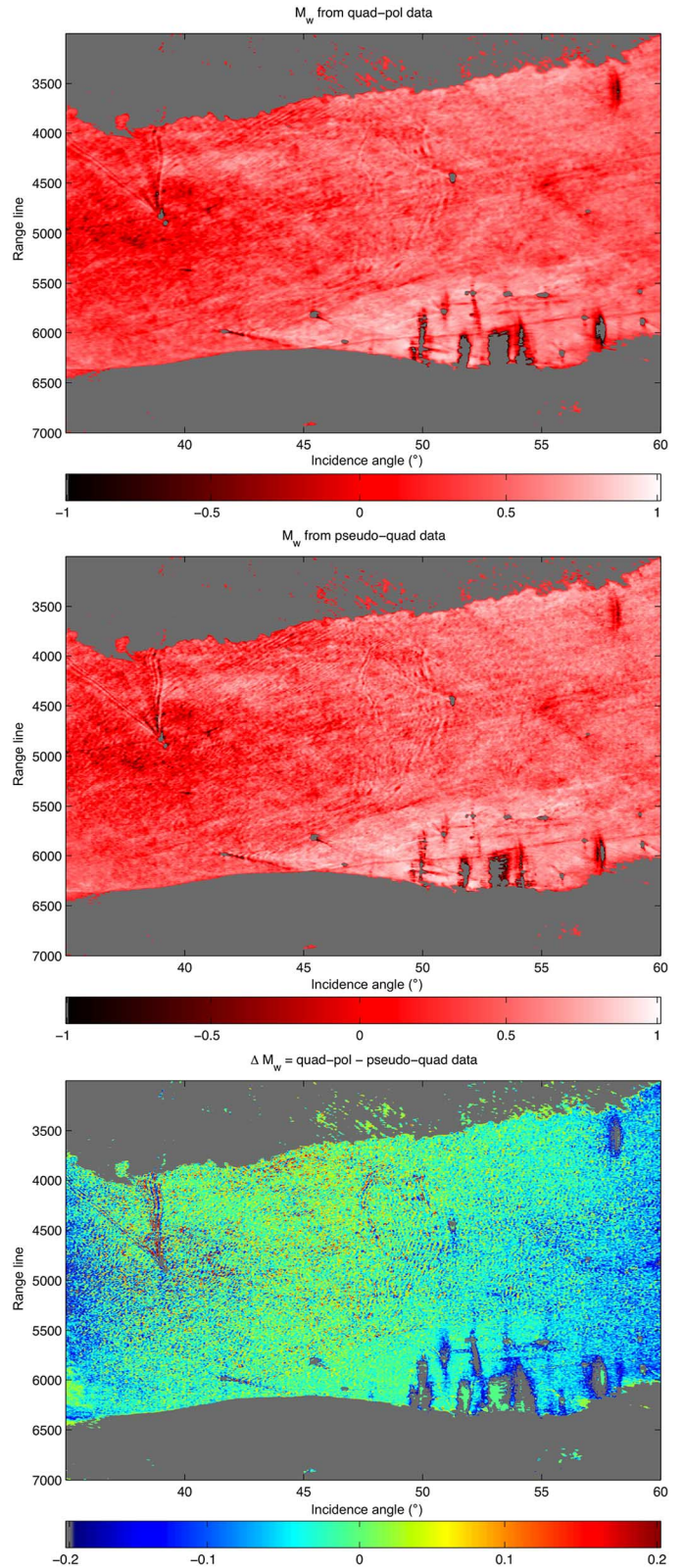


Fig. 9. Images of M_W for quad-pol data (top) and reconstructed pseudo-quad data (center). The difference image is shown at bottom.

The M_α values all fall between 0 and 1. The mean for the quad-pol data is 0.34 and for the pseudo-quad data is 0.30. One can see that the pseudo-quad data reproduce the shape of the quad-pol histogram. The mean difference is 0.04, and

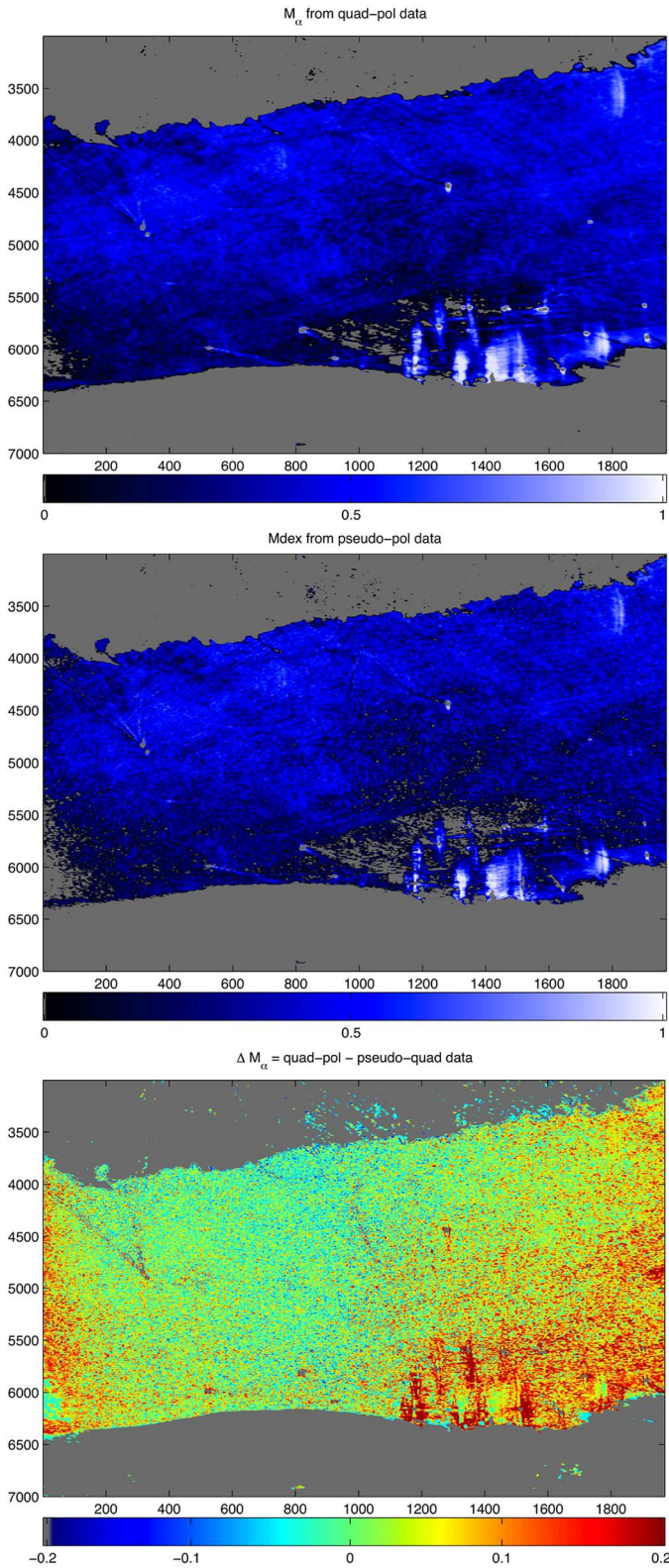


Fig. 10. Images of M_α for quad-pol data (top) and reconstructed pseudo-quad data (center). The difference image is shown at bottom.

the RMSE is 0.083; thus, the pseudo-quad provides a reliable estimate of the M_α term. The spatial patterns in the quad-pol M_α are reproduced in the pseudo-quad image. The histogram of the difference image shows that the pseudo-quad underestimates M_α slightly. This is visible in the difference

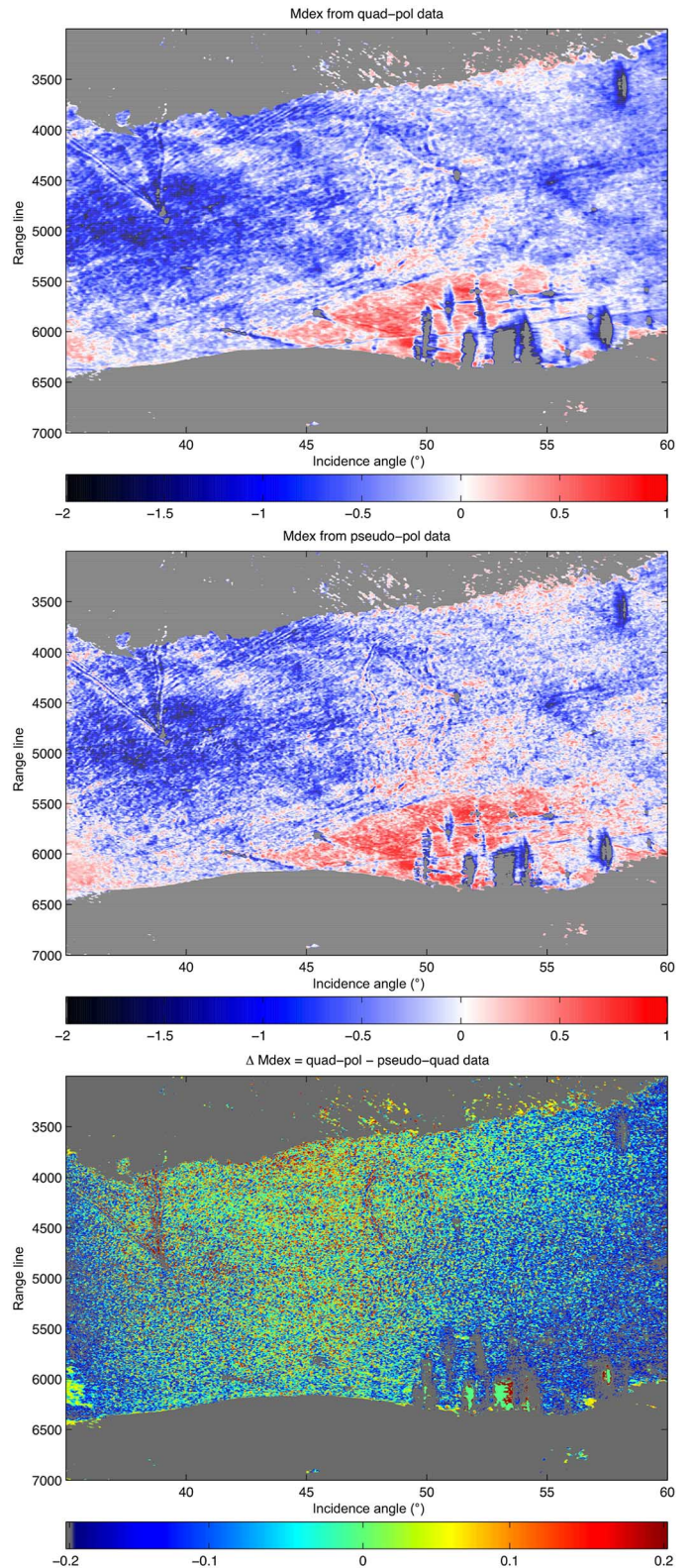


Fig. 11. Images of M_{dex} for quad-pol data (top) and reconstructed pseudo-quad data (center). The difference image is shown at bottom.

image which again shows a slight increase in difference for low and high incidence angles.

The M_{dex} histogram has the same Gaussian shape as seen in [11]. The mean M_{dex} for the quad-pol data is 0.07 and for the pseudo-quad data is 0.14. The mean difference is -0.07 and the

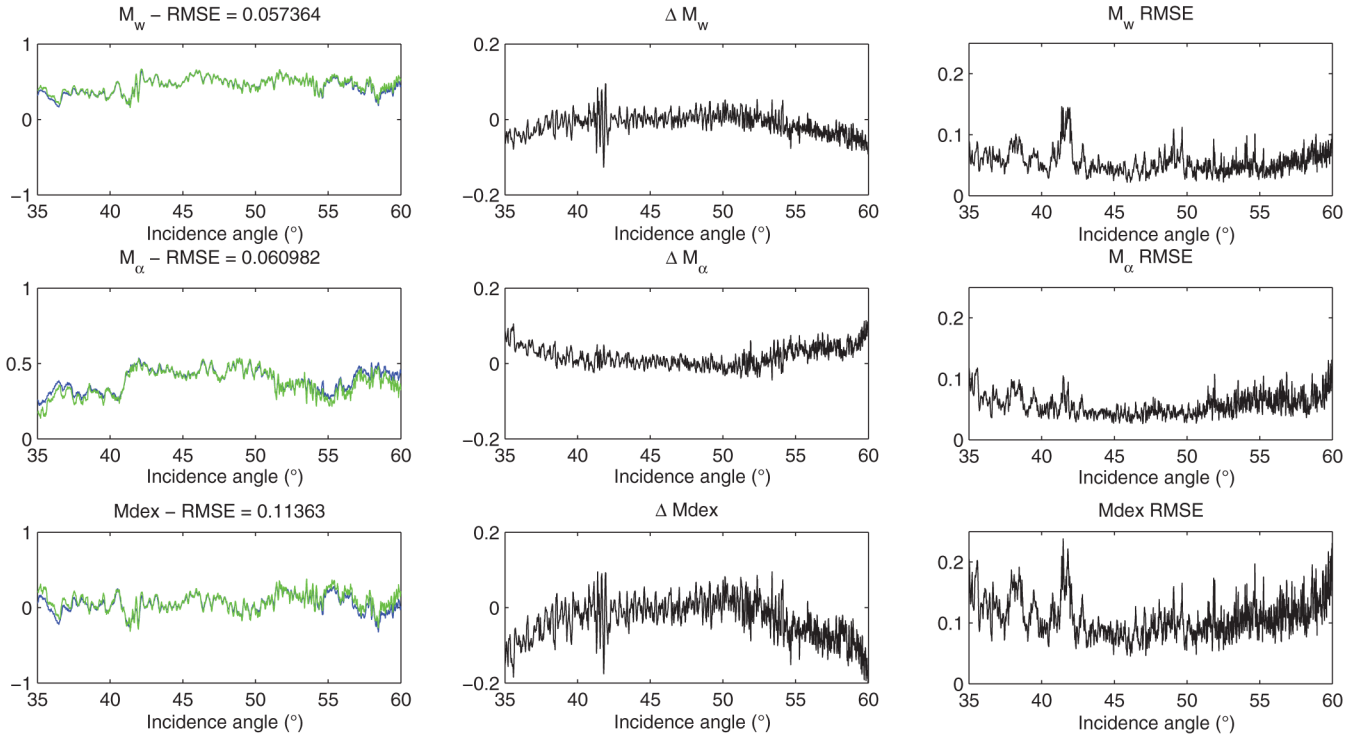


Fig. 12. Mean transects of M_W , M_α , and M_{dex} calculated from lines 4300 to 4400. The plots on the left show mean transects of quad-pol data (blue) and reconstructed pseudo-quad data (green). The plots in the center show the mean difference between quad-pol and pseudo-quad indices ($\Delta = \text{quad-pol} - \text{pseudo-quad}$) and the plots on the right show the RMSE.

RMSE is 0.16. One can see from the histogram of ΔM_{dex} that the reconstructed pseudo-quad data overestimate M_{dex} slightly as one would expect since the M_W component is overestimated and the M_α is underestimated. The M_{dex} images show that the spatial patterns in the quad-pol data are reproduced in the pseudo-quad image. In the difference image, we can again see an increase of the difference with incidence angle. This increase is slightly more than the two components as they are “constructively interfering.”

We also provide mean range transects of M_W , M_α , and M_{dex} in Fig. 12 for azimuth lines 4300–4400, corresponding to a section of the oil slick. These transects provide a clearer view of the incidence angle dependence of M_{dex} and its components. In choosing these azimuth lines, we have deliberately avoided the patch of what appears to be wind-roughened oil slick between lines 4600 and 5500 and incidence angles 30° and 40° . This appears as dark patches in the M_W images in Fig. 9, where the roughness of the oil slick exceeds the roughness of the selected patch of clean water. One can see that the value of M_W still dips below zero in places indicating that the local roughness of the oil covered water exceeds that of the clean water.

Fig. 12 shows that the values of M_W , M_α , and M_{dex} are approximately constant with incidence angle. The mean difference transects show a definite incidence angle dependence—relatively constant between 40° and 50° and increasing/decreasing at angles less than 40° and greater than 50° . The sign of the differences in M_W and M_α combine constructively to increase the difference in M_{dex} .

The incidence angle dependence in the mean difference is much weaker in the RMSE. The error in M_{dex} and its two

components is approximately constant with incidence angle, although it does appear to increase slightly starting at 50° , mirroring the increase in σ_{HH}^0 error. Unlike the two components, the M_{dex} error seems to increase slightly below about 45° . This slight increase is also consistent with the slight increase in σ_{HH}^0 error for the same incidence angle range. Although there are several spikes in the error in M_{dex} , it is mostly below 0.1.

Finally, we performed similar processing on pass 32 010, and similarly measured the errors in M_W , M_α , and M_{dex} for the pseudo-quad data. Since pass 32 010 was not used to estimate the value of N_{ra} and the reflection asymmetry terms (we used the same values as for pass 14 010), we would expect the results to be slightly worse. The estimate of M_w had a mean error of 0.11, and RMSE of 0.14. M_α had a mean error of -0.054 and RMSE of 0.065. The M_{dex} had a mean error of 0.16 and RMSE of 0.20. We note that the mean errors of M_W and M_{dex} have increased compared to pass 14 010. However, the overall RMSE of 0.20 is still reasonable, and despite the bias, the pseudo-quad data captures the majority of the variance in the quad-pol M_{dex} . Most of the error is contained in the estimate of M_W .

IV. CONCLUSION

We have shown that co-pol SAR data reconstructed from simulated compact polarity has errors that are low enough to be able to calculate an M_{dex} oil–water mixing index that is operationally equivalent to that calculated from the original quad-pol data.

In this study, reflection asymmetry was a significant barrier to accurately reconstructing linear-pol data from the simulated

compact polarity images, which was quite different from our experience working with Radarsat-2 fine-quad data. To carry out the linear-pol reconstruction on the UAVSAR data, we developed a refined model of the reconstruction parameter N versus incidence angle for an oil-free subset of water in pass 14 010. This model produced estimates of σ_{VV}^0 with errors less than 0.1 dB, σ_{HH}^0 with errors less than 0.2 dB up to about 55° , and σ_{HV}^0 with errors less than 0.5 dB.

We used these reconstructed data to calculate the oil/water mixing index as proposed by Minchew [11]. The mean difference between the quad-pol and pseudo-quad Mdex values is -0.09 , and in general, the images of M_W , M_α , and Mdex show that the general trend of the quad-pol parameters is preserved by the pseudo-quad data. The mean range transects of Mdex also show a good correspondence between quad-pol and pseudo-quad Mdex values, with very small errors. These transects reveal the challenge of reconstructing quad-pol data from CP data for such a large range of incidence angles. The errors in the Mdex estimate increases at both low (below 40°) and high (above 50°) incidence angles.

While the pseudo-quad data appears to slightly overestimate Mdex for incidence angles less than 40° and greater than 50° , the pseudo-quad data captures the spatial patterns of the oil–water index, in particular, the pattern in the area of positive (thin oil film) and negative (oil–water mixture) Mdex. Overall, the pseudo-quad data provide an excellent estimate of Mdex, and thus, the CP SAR shows promise in this application.

Although the cross-pol backscatter was not used in this work, our refined reconstruction algorithm provides an excellent estimate of σ_{HV}^0 , which may be used for other aspects of maritime surveillance, including wind speed estimation [34]. The algorithm also provides an estimate of the relative HH–VV phase difference, which has also shown potential for oil detection and characterization applications [9]. When combined with our previous work on ship detection [23] and iceberg detection [22], this work suggests that CP SAR is an excellent instrument for maritime surveillance, combining greater polarization diversity than standard linear dual-pol data, with the wide swath imaging that is essential for monitoring the ocean.

APPENDIX

We explored the validity of the assumption of reflection symmetry in the UAVSAR data by comparing the comparable elements of the third component of the CTLR covariance matrix [see (3)] with the first and second components. Thus, we examined the following ratios:

$$\frac{-2\mathcal{I}(\langle S_{HH}S_{HV}^* \rangle)}{(\langle |S_{HH}|^2 \rangle + \langle |S_{HV}|^2 \rangle)} \quad (24)$$

$$\frac{2\mathcal{I}(\langle S_{VV}S_{HV}^* \rangle)}{(\langle |S_{VV}|^2 \rangle + \langle |S_{HV}|^2 \rangle)} \quad (25)$$

$$\frac{|\langle S_{HH}S_{HV}^* \rangle + \langle S_{HV}S_{VV}^* \rangle|}{|\langle S_{HH}S_{VV}^* \rangle - \langle |S_{HV}|^2 \rangle|} \quad (26)$$

The mean values of these ratios as a function of the number of samples are shown in Fig. 13. The columns represent the

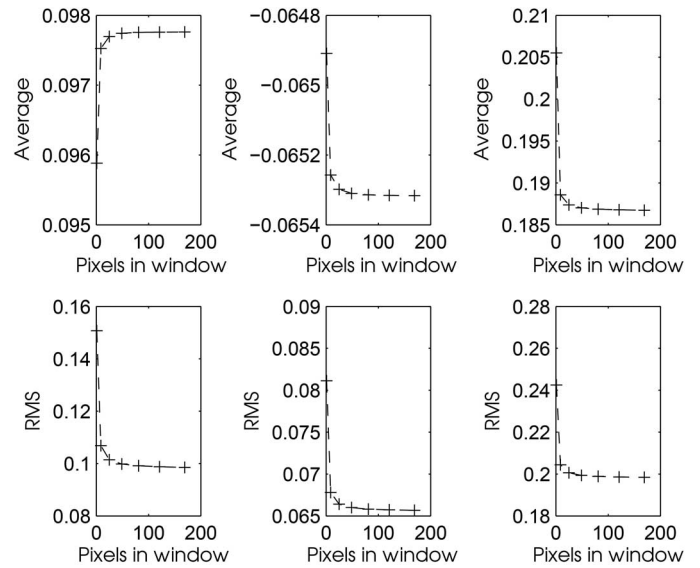


Fig. 13. Plots showing the amount of reflection asymmetry in the 14 010 water subset. The left plot shows the RMS of the quantity $-2\mathcal{I}(\langle S_{HH}S_{HV}^* \rangle) / (\langle |S_{HH}|^2 \rangle + \langle |S_{HV}|^2 \rangle)$, where angle brackets denote spatial averaging. The middle plot shows the quantity $2\mathcal{I}(\langle S_{VV}S_{HV}^* \rangle) / (\langle |S_{VV}|^2 \rangle + \langle |S_{HV}|^2 \rangle)$. The right plot shows the quantity $|\langle S_{HH}S_{HV}^* \rangle + \langle S_{HV}S_{VV}^* \rangle| / |\langle S_{HH}S_{VV}^* \rangle - \langle |S_{HV}|^2 \rangle|$. The x-axis shows the number of pixels included in the spatial averaging window—greater spatial averaging tends to increase reflection symmetry, up to a certain threshold. For a perfectly reflection symmetric dataset, all of the above quantities would equal zero.

three different ratios: ratio 24 is shown in the left-hand column, ratio 25 in the center, and ratio 26 in the right-hand column. As observed by Souyris *et al.* [16], ratio 26 is the largest. Our values are higher than the L-band results presented by Souyris, the difference being the higher spatial resolution of the UAVSAR. In this work, we use a 5×5 -pixel window for the necessary spatial averaging. Fig. 13 suggests that larger averaging windows will not reduce the effects of reflection asymmetry any further.

ACKNOWLEDGMENT

C. Jones and B. Holt performed this work at the Jet Propulsion Laboratory, California Institute of Technology, under contract with the National Aeronautics and Space Administration.

REFERENCES

- [1] C. Brekke and A. H. S. Solberg, "Oil spill detection by satellite remote sensing," *Remote Sens. Environ.*, vol. 95, no. 1, pp. 1–13, 2005.
- [2] G. D. Carolis, M. Adamo, and G. Pasquariello, "On the estimation of the thickness of marine oil slicks from sun-glittered, near-infrared MERIS and MODIS imagery: The Lebanon oil spill case study," *IEEE Trans. Geosci. Remote Sens.*, vol. 52, no. 1, pp. 559–573, Jan. 2014.
- [3] R. F. Kokaly *et al.*, "Spectroscopic remote sensing of the distribution and persistence of oil from the Deepwater Horizon spill in Barataria Bay marshes," *Remote Sens. Environ.*, vol. 129, pp. 210–230, 2013.
- [4] D. Casciello, T. Lacava, N. Pergola, and V. Tramutol, "Robust satellite techniques for oil spill detection and monitoring using AVHRR thermal infrared bands," *Int. J. Remote Sens.*, vol. 32, no. 14, pp. 4107–4129, 2011.
- [5] J. W. Wright, "Backscattering from capillary waves with application to sea clutter," *IEEE Trans. Antennas Propag.*, vol. AP-14, no. 6, pp. 749–754, Nov. 1966.

- [6] W. Alpers and H. Hühnerfuss, "The sampling of ocean waves by surface films: A new look at an old problem," *J. Geophys. Res.*, vol. 94, no. C5, pp. 6251–6265, 1989.
- [7] F. Nunziata, A. Gabardella, and M. Migliaccio, "On the mueller scattering matrix for SAR sea oil slick observation," *IEEE Geosci. Remote Sens. Lett.*, vol. 5, no. 4, pp. 691–695, Oct. 2008.
- [8] M. Migliaccio, A. Gambardella, and M. Tranfaglia, "SAR polarimetry to observe oil spills," *IEEE Trans. Geosci. Remote Sens.*, vol. 45, no. 2, pp. 506–511, Feb. 2007.
- [9] M. Migliaccio, F. Nunziata, and A. Gambardella, "On the co-polarized phase difference for oil spill observation," *Int. J. Remote Sens.*, vol. 30, no. 6, pp. 1587–1602, 2009.
- [10] B. Minchew, C. Jones, and B. Holt, "Polarimetric analysis of backscatter from the Deepwater Horizon oil spill using L-band synthetic aperture radar" *IEEE Trans. Geosci. Remote Sens.*, vol. 50, no. 10, pp. 3812–3930, Oct. 2012.
- [11] B. Minchew, "Determining the mixing of oil and sea water using polarimetric synthetic aperture radar," *Geophys. Res. Lett.*, vol. 39, pp. 1–6, 2012.
- [12] R. K. Raney, "Hybrid-polarity SAR architecture," *IEEE Trans. Geosci. Remote Sens.*, vol. 45, no. 11, pp. 3397–3404, Nov. 2007.
- [13] R. K. Raney *et al.*, "The lunar Mini-RF radars: Hybrid polarimetric architecture and initial results," *Proc. IEEE*, vol. 99, no. 5, pp. 808–823, May 2011.
- [14] L. Carter, D. Campbell, and B. Campbell, "Geologic studies of planetary surfaces using radar polarimetric imaging," *Proc. IEEE*, vol. 99, no. 5, pp. 770–782, May 2011.
- [15] R. K. Raney, J. T. S. Cahill, G. W. Patterson, and D. B. J. Bussey, "The m-chi decomposition of hybrid dual-polarimetric radar data with application to lunar craters," *J. Geophys. Res.*, vol. 117, no. E12, p. E00H21, 2012.
- [16] J.-C. Souyris, P. Imbo, R. Fjortoft, S. Mingot, and J.-S. Lee, "Compact polarimetry based on symmetry properties of geophysical media: The $\pi/4$ mode," *IEEE Trans. Geosci. Remote Sens.*, vol. 43, no. 3, pp. 634–646, Mar. 2005.
- [17] T. Ainsworth, J. Kelly, and J.-S. Lee, "Classification comparisons between dual-pol, compact polarimetric and quad-pol SAR imagery," *ISPRS J. Photogramm. Remote Sens.*, vol. 64, pp. 464–471, 2009.
- [18] M.-L. Truong-Loi, A. Freeman, P. Dubois-Fernandez, and E. Pottier, "Estimation of soil moisture and faraday rotation from bare surfaces using compact polarimetry," *IEEE Trans. Geosci. Remote Sens.*, vol. 47, no. 11, pp. 3608–3615, Nov. 2009.
- [19] S. Angelliaume, P. Dubois-Fernandez, and J.-C. Souyris, "Compact polinsar for vegetation characterisation," in *Proc. IEEE Int. Geosci. Remote Sens. Symp. (IGARSS)*, 2007, pp. 1136–1138.
- [20] C. Lardeux *et al.*, "Classification of tropical vegetation using multifrequency partial SAR polarimetry," *IEEE Geosci. Remote Sens. Lett.*, vol. 8, no. 1, pp. 133–137, Jan. 2011.
- [21] M. Nord, T. Ainsworth, J.-S. Lee, and N. Stacy, "Comparison of compact polarimetric synthetic aperture radar modes," *IEEE Trans. Geosci. Remote Sens.*, vol. 47, no. 1, pp. 174–188, Jan. 2009.
- [22] M. Denbina and M. J. Collins, "Iceberg detection using pseudo quad-pol reconstruction of compact polarimetric SAR," *Atmos. Ocean*, vol. 50, no. 4, pp. 437–446, 2012.
- [23] G. Atteia and M. J. Collins, "On the use of compact polarimetry SAR for ship detection," *ISPRS J. Photogramm. Remote Sens.*, vol. 80, pp. 1–9, 2012.
- [24] B. Zhang, W. Perriea, X. Li, and W. G. Pichel, "Mapping sea surface oil slicks using RADARSAT-2 quad-polarization SAR image," *Geophys. Res. Lett.*, vol. 38, no. 10, p. L10602, 2011.
- [25] A. B. Salberg, O. Rudjord, and A. H. S. Solberg, "Oil spill detection in hybrid-polarimetric SAR images," *IEEE Trans. Geosci. Remote Sens.*, vol. 52, no. 10, pp. 6521–6533, Oct. 2014.
- [26] C. Brekke, B. Holt, C. Jones, and S. Skrunes, "Discrimination of oil spills from newly formed sea ice by synthetic aperture radar," *Remote Sens. Environ.*, vol. 145, pp. 1–14, 2014.
- [27] R. Shirvany, M. Chabert, and J.-Y. Tourneret, "Ship and oil-spill detection using the degree of polarization in linear and hybrid/compact dual-pol SAR," *IEEE J. Sel. Topics Appl. Earth Observ. Remote Sens.*, vol. 5, no. 3, pp. 885–892, Jun. 2012.
- [28] A. Iodice, A. Natale, and D. Riccio, "Retrieval of soil surface parameters via a polarimetric two-scale model," *IEEE Trans. Geosci. Remote Sens.*, vol. 49, no. 7, pp. 2531–2547, Jul. 2011.
- [29] M. Collins, M. Denbina, and G. Atteia, "On the reconstruction of quad-pol SAR data from compact polarimetry data for ocean target detection," *IEEE Trans. Geosci. Remote Sens.*, vol. 51, no. 1, pp. 591–600, Jan. 2013.
- [30] C. E. Jones, B. Minchew, and B. Holt, "Studies of the deepwater horizon oil spill with the UAVSAR radar," in *Monitoring and Modeling the Deepwater Horizon Oil Spill: A Record-Breaking Enterprise*, vol. 195, Y. Liu, A. Macfadyen, Z.-G. Ji, and R. H. Weisberg, Eds. Washington DC, USA: American Geophysical Union, 2011, pp. 33–50.
- [31] P. Rosen *et al.*, "UAVSAR: New NASA airborne SAR system for research," *IEEE Aerosp. Electron. Syst. Mag.*, vol. 22, no. 11, pp. 21–28, Nov. 2007.
- [32] S. V. Nghiem, S. H. Yueh, R. Kwok, and F. K. Li, "Symmetry properties in polarimetric remote sensing," *Radio Sci.*, vol. 27, no. 5, pp. 693–711, 1992.
- [33] S. Yueh, S. Nghiem, and R. Kwok, "Comparison of a polarimetric scattering and emission model with ocean backscatter and brightness measurements," in *Proc. IEEE Int. Geosci. Remote Sens. Symp. (IGARSS)*, 1994, vol. 1, pp. 258–260.
- [34] P. Vachon and J. Wolfe, "C-band cross-polarization wind speed retrieval," *IEEE Geosci. Remote Sens. Lett.*, vol. 8, no. 3, pp. 456–459, May 2011.
- [35] G. R. Valenzuela, "Theories for the interaction of electromagnetic and ocean waves—A review," *Boundary Layer Meteorol.*, vol. 13, no. 1–4, pp. 61–85, 1978.
- [36] G. R. Valenzuela, "Scattering of electromagnetic waves from a tilted slightly rough surface," *Radio Sci.*, vol. 3, no. 6, pp. 1057–1066, 1968.
- [37] G. R. Valenzuela, M. B. Laing, and J. C. Daley, "Ocean spectra for the high frequency waves as determined from airborne radar measurements," *J. Mar. Res.*, vol. 29, pp. 69–84, 1971.
- [38] F. Ulaby, R. Moore, and A. Fung, "Microwave remote sensing: Active and passive," in *Scattering and Emission Theory*, vol. 3. Norwood, MA, USA: Artech House, Inc., 1986.
- [39] B. Fiscella, A. Giancaspro, F. Nirchio, P. Pavese, and P. Trivero, "Oil spill detection using marine SAR images," *Int. J. Remote Sens.*, vol. 21, no. 18, pp. 3561–3566, 2000.
- [40] K. Folgero, "Bilinear calibration of coaxial transmission/reflection cells for permittivity measurement of low-loss liquids," *Meas. Sci. Technol.*, vol. 7, no. 9, pp. 1260–1269, 1996.
- [41] L. Klein and C. Swift, "An improved model for the dielectric constant of sea water at microwave frequencies," *IEEE J. Oceanic Eng.*, vol. 2, no. 1, pp. 104–111, Jan. 1977.



Michael J. Collins (S'87–M'93–SM'00) received the B.Sc.Eng. degree in survey engineering from the University of New Brunswick, Fredericton, NB, Canada, in 1981, the M.Sc. degree in physical oceanography from the University of British Columbia, Vancouver, BC, Canada, in 1987, and the Ph.D. degree in earth and space science from York University, Toronto, ON, Canada, in 1993.

He is a Faculty Member with the Department of Geomatics Engineering, University of Calgary, Calgary, AB, Canada. He has also been a Faculty Member with the Department of Survey Engineering, University of Maine, Orono, ME, USA, and with the Department of Geodesy and Geomatics Engineering, University of New Brunswick; a Project Scientist with the Institute for Space and Terrestrial Science, Toronto, ON, Canada, and an Engineer with McElhanney Group in Vancouver and Calgary. He has also served as a Consultant to government and industry on various aspects of remote sensing. He has spent sabbatical years in the Department of Electrical and Computer Engineering, University of Texas at Austin, Austin, TX, USA, in 2006 and 2007, and in the Climate, Oceans, and Solid Earth Sciences section at the Jet Propulsion Lab, Pasadena, CA, USA, in 2011 and 2012. His research interests include several aspects of radar remote sensing, including polarimetric analysis, simulation of signal data, texture analysis, segmentation, classification and target detection, estimation of forest, ocean, and sea ice characteristics and the fusion of radar with electro-optical and other geospatial data.



Michael Denbina (S'11) received the B.Sc. degree in electrical engineering from the University of Calgary, Calgary, AB, Canada, in 2010, and the Ph.D. degree in geomatics engineering from the University of Calgary, in 2015.

His research interests include the use of radar remote sensing for a variety of applications such as forest monitoring, wind speed estimation, oil spill monitoring, and ocean target discrimination.



Brent Minchew received the B.S. and M.S. degrees in aerospace engineering from the University of Texas at Austin, Austin, TX, USA, in 2008 and 2010, respectively. Currently, he is working toward the Ph.D. degree in geophysics at the California Institute of Technology, Pasadena, CA, USA.

During summer 2009 and summer 2010, he was a Graduate Research Assistant with the Uninhabited Aerial Vehicle Synthetic Aperture Radar Group, NASA's Jet Propulsion Laboratory, La Cañada Flintridge, CA, USA. From 1996 to 2004, he served

on active duty in the U.S. Marine Corps. During that time, he was assigned to the Presidential Helicopter Squadron HMX-1, Marine Heavy Helicopter Squadron HMM-461, and HMM-264 as part of the 26th Marine Expeditionary Unit. As an undergraduate, he researched high energy electromagnetic launchers at the Institute for Advanced Technology. His research interests include glaciers with an emphasis on remote sensing techniques.



Cathleen E. Jones received the B.S. degree in physics from Texas A&M University, College Station, TX, USA, and the Ph.D. degree in physics from the California Institute of Technology, Pasadena, CA, USA.

She is a Radar Scientist and Engineer with NASA's Jet Propulsion Laboratory, La Cañada Flintridge, CA, USA. Her research interests include SAR remote sensing for studying natural disasters and monitoring critical infrastructure.



Benjamin Holt received the B.S. degree from Stanford University, Stanford, CA, USA, in 1972, and the M.S. degree in physical oceanography from the University of Southern California, Los Angeles, CA, USA, in 1988.

He is a Research Scientist with Earth Science Section, Oceans and Ice Group, Jet Propulsion Laboratory, California Institute of Technology, Pasadena, CA, USA, which he joined in 1978. His research interests include using multisensor remote sensing data to examine the geophysical state of

polar sea ice and snow, coastal oceanography circulation, the detection of marine pollutants, new instrument development, and techniques for microwave measurement of sea ice thickness.